Journal Pre-proof

Large-area SERS chip based on periodic striped metal-insulator-metal structures fabricated by laser interference lithography

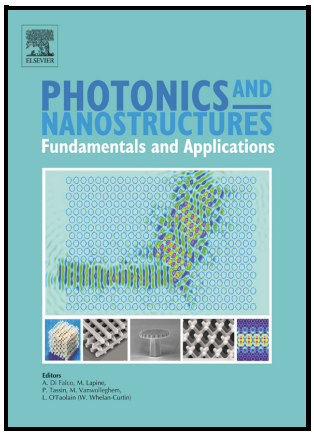

Litong Dong, Xuanyi Dong, Yue Wang, Mengnan Liu, Wenmin Zhang, Lu Wang, Dayou Li, Wilhelm Pfleging, Zuobin Wang

PII: S1569-4410(26)00156-2

DOI: https://doi.org/10.1016/j.photonics.2026.101656

Reference: PNFA101656

To appear in: *Photonics and Nanostructures - Fundamentals and Applications*

Received date: 14 July 2026
Revised date: 20 September 2026
Accepted date: 15 October 2026

Please cite this article as: Litong Dong, Xuanyi Dong, Yue Wang, Mengnan Liu, Wenmin Zhang, Lu Wang, Dayou Li, Wilhelm Pfleging and Zuobin Wang, Large-area SERS chip based on periodic striped metal-insulator-metal structures fabricated by laser interference lithography, *Photonics and Nanostructures - Fundamentals and Applications,* (2026) doi:https://doi.org/10.1016/j.photonics.2026.101656

This is a PDF of an article that has undergone enhancements after acceptance, such as the addition of a cover page and metadata, and formatting for readability. This version will undergo additional copyediting, typesetting and review before it is published in its final form. As such, this version is no longer the Accepted Manuscript, but it is not yet the definitive Version of Record; we are providing this early version to give early visibility of the article. Please note that Elsevier's sharing policy for the Published Journal Article applies to this version, see: https://www.elsevier.com/about/policies-and-standards/sharing#4-published-journal-article. Please also note that, during the production process, errors may be discovered which could affect the content, and all legal disclaimers that apply to the journal pertain.

Large-area SERS chip based on periodic striped metal-insulator-metal structures fabricated by laser interference lithography

Litong Dong [a, b *], Xuanyi Dong [a, b], Yue Wang [a, b], Mengnan Liu [a,c] *, Wenmin Zhang [a, b], Lu Wang [a], Dayou Li [d], Wilhelm Pfleging [e], and Zuobin Wang [a, b, d].

a. JR3CN&CNM, Changchun University of Science and Technology, Changchun, China.

b. Zhongshan Institute of Changchun University of Science and Technology, Zhongshan, China.

c. Key Laboratory of Architectural Cold Climate Energy Management, Ministry of Education,

Jilin Jianzhu University, 5088 Xincheng Street, Changchun, 130118, China

d. JR3CN&IRAC, University of Bedfordshire, Luton, UK.

e. IAM-AWP, Karlsruhe Institute of Technology, Eggenstein-Leopoldshafen, Germany.

*donglt@cust.edu.cn

*mengnanliu07@126.com

Journal Pre-proof

Abstract

Large-area, low-cost, good-reliability, and high-sensitivity surface-enhanced Raman scattering (SERS) substrate is a prerequisite for such devices to enter the market. In this work, we present a SERS substrate consisting of a vertical metal-insulator-metal (MIM) nano-stripe pattern fabricated by laser interference lithography (LIL). The proposed SERS substrate exhibits high sensitivity, reproducibility, and stability, with the characteristic Raman signals of rhodamine 6G (R6G) experimentally detected at concentrations down to 10^{-8} M and an enhancement factor (EF) exceeding 10^{10}. Furthermore, by integrating the SERS substrate with a microfluidic chip enabled the construction of a real-time, in situ and non-destructive detection device, whose SERS performance was validated via Raman spectra tests of melamine and malachite green. Overall, this work comes up with an efficient strategy for fabricating sensitive and reproducible SERS substrates that hold considerable promise for advancing biochemical sensors equipped with SERS functionality.

Keywords

Laser interference lithography, SERS, Metal-insulator-metal structures, Microfluidic, Period micro-nano structures.

1. Introduction

Surface-enhanced Raman scattering (SERS) is widely recognized as a non-destructive and ultra-sensitive vibrational spectroscopy technique for trace analyte identification in various fields, including food safety regulation [1, 2], environmental monitoring [3, 4], chemical molecular identification [5, 6], and DNA analysis [7, 8]. An ideal SERS substrate should provide strong signal enhancement, highly uniform, good reproducibility, and a simple fabrication process [9]. The development of low-cost SERS substrates with high sensitivity is of great significance for the application and advancement of SERS technology. Electromagnetic enhancement, which originates from the collective oscillation of conduction electrons induced by incident light on metal surfaces, is generally considered the dominant mechanism responsible for SERS enhancement [10]. Based on this mechanism, considerable efforts have been devoted to the design and fabrication of micro/nanostructures with strong electromagnetic field confinement and high-density "hotspots" [11].

To strengthen local electromagnetic fields, nanostructures with nanoscale gaps, such as homodimers [12], heterodimers [13], trimers [14], and heterogeneous structures [15], have been extensively investigated. Compared with planar nanopatterns, metal-insulator-metal sandwich nanostructures can generate broadband and multi-resonant plasmonic hotspots with strong spatial localization [16]. Among them, metal-insulator-metal (MIM) nanostructures offer unique spatial mode distributions and have shown great potential in various applications [17-18], particularly in SERS sensing. For example, vertically stacked Au/SiO_2-nanolaminated structures support multiple hybridized localized surface plasmon modes, enabling multi-resonant optical concentration and improved spectral matching with excitation wavelengths under varying background refractive indices [19]. Similarly, Ag/SiO_2/Ag laminated plasmonic nanocavities on the nanopillar arrays can achieve high SERS enhancement over a wide spectral range, producing uniform and reproducible multiband SERS signals through precise control of vertical plasmonic nanogaps [20]. Owing to multidimensional plasmonic coupling at metal-dielectric interfaces, Si nanopillars coated with Au/Ta_2O_5/Au exhibit stronger Raman enhancement than those coated with a single metal layer [21]. Although MIM structures have been widely explored for SERS applications, their fabrication processes are often complex, costly, and time-consuming, which limits their practical application. Therefore, the development of high-throughput, simple, and efficient fabrication strategies for large-area, low-cost, stable, and user-friendly SERS devices remains an important research focus.

Laser-based processing provides a versatile approach to fabricating micro- and nanostructured functional surfaces. Geng et al. used machine learning to optimize micro-groove geometry in nanosecond laser processing [22]. Mikalkevičius et al. combined femtosecond (fs) laser induced periodic structures on silicon with Ag nanoparticle deposition for SERS sensing [23]. For large-area periodic patterning, laser interference lithography (LIL) records optical interference patterns in photoresist, enabling geometric control through the interference configuration and exposure conditions. Jiang et al. demonstrated centimeter-scale periodic nanostructures using deep-ultraviolet LIL with flat-top beam shaping [24]. Together, these studies highlight the potential of laser-based processing for controllable surface structuring, integration with functional materials, and large-area fabrication. LIL combines periodic patterning with geometric tunability and compatibility with thin-film deposition, providing a suitable route for the large-area fabrication of multilayer SERS substrates.

In this work, we proposed periodic striped MIM structures for SERS sensing and employed two-beam LIL combined with thin-film deposition for their large-area fabrication. FDTD simulations were conducted to investigate the electric-field distributions and absorption spectra of various structural configurations and to analyze their SERS performance. Furthermore, by integrating the SERS substrate with a microfluidic chip, a SERS-microfluidic platform was developed for proof-of-concept molecular sensing, demonstrating enhanced Raman signals and good signal consistency.

2. Materials and Methods

2.1 FDTD Simulation

The structural simulation of the SERS substrate was conducted using the FDTD method. A 532 nm plane wave was adopted as the incident light source, and frequency-domain field and power monitors were used to acquire the electric field distribution in the X-Z plane. Periodic boundary conditions were applied along the X direction, while perfectly matched layers (PML) were set for the Y and Z directions. The mesh size was set to 3.6 nm × 3.6 nm × 3.6 nm.

2.2 Materials

Single-side polished undoped silicon wafers were purchased from Zhejiang Lijing Co., Ltd., while photoresist (PR) (AR-P 3740) and developer (AR 300-47) were obtained from Allresist GmbH. This original solution was diluted at a ratio of 1:1 using a diluent

(propylene glycol monomethyl ether acetate) procured from Shanghai Aladdin Biochemical Technology Co., Ltd. Rhodamine 6G, malachite green and melamine were all sourced from Shanghai Maclin Biochemical Technology Co., Ltd.

2.3 Characterization Methods

The morphology and Raman spectra were characterized using a scanning electron microscope (MEGNA, TESCAN) and a Raman spectrometer (LabRAM Odyssey, HORIBA). The metal films were fabricated utilizing magnetron sputtering equipment (Q150TES, Quorum Technologies Ltd.). The insulating layer was fabricated using a plasma deposition system (SENTECH, SI 500D). Raman spectra tests were performed after immersing the samples in the probe solution for 2 h, the excitation wavelength at 532 nm, the polarization direction of incident light as p-polarized, and the excitation power at 3.9 mW. A 10X objective lens was used to focus the laser on the sample surface, and Raman signals were collected in backscattering mode with an integration time of 1 s and 5 accumulations. For melamine detection, the integration time was extended to 10 s with 10 accumulations. R6G aqueous solution was used as the probe molecule, with characteristic Raman peaks at 610 cm^{-1}, 773 cm^{-1}, 1185 cm^{-1}, and 1363 cm^{-1} correspond to C-C-C in-plane bending, C-H out-of-plane bending, C-H in-plane bending, and C-C stretching vibrations, respectively.

3 Fabrication of the periodic striped MIM structures

The fabrication process of the periodic striped MIM structures is illustrated in Fig. 1a. A 50-nm-thick Au layer is deposited on the silicon substrate by physical vapor deposition (PVD) via vacuum evaporation at the room temperature under a chamber pressure of 3×10^{-6} Torr, with an evaporation rate of 1 Å/s and a substrate rotation speed of 20 rpm. Subsequently, a 20-nm-thick SiO_2 layer is deposited on the Au layer by plasma-enhanced chemical vapor deposition (PECVD) at 260 ℃, with an ICP power of 700 W and the gas flow rates of 131, 10, and 126 sccm for SiH_4, O_2, and Ar, respectively. A photoresist (PR) layer is spin-coated onto the sample surface, followed by the two-beam LIL system exposure, development, and rinsing to form the stripe pattern. Finally, a 30-nm-thick Ag layer is deposited via PVD sputtering under a sputtering current of 70 mA, a chamber pressure of 9.8×10^{-3} Torr, and a tooling factor of 2.3, completing the striped Ag/SiO_2/Au structures shown in Fig. 1b. Energy dispersive spectroscopy (EDS) analysis confirms the presence of Au and Ag in the structure, with both elements uniformly distributed on the surface, as shown in Figs. 1c-d.

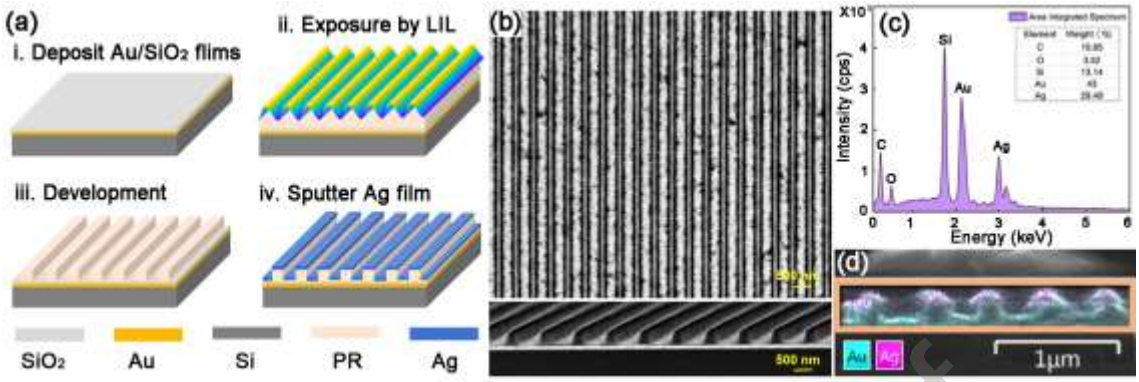

Fig. 1 (a) Flow chart of the fabrication procedures for periodic striped MIM structures. (b) SEM images of the sample prepared by the two-beam LIL system. (c) EDS spectrum of the periodic striped MIM structure. (d) EDS mapping of the Au and Ag elements.

In this fabrication process, a single-longitudinal-mode laser (Genesis CX355-100 SLM, COHERENT) with an output wavelength of 355 nm is incorporated into the two-beam LIL system. The morphological changes in line width and height corresponding to different development time, RP thickness and exposure doses due to nonlinear effects inherent to photoresists [25, 26], as shown in Fig. 2.

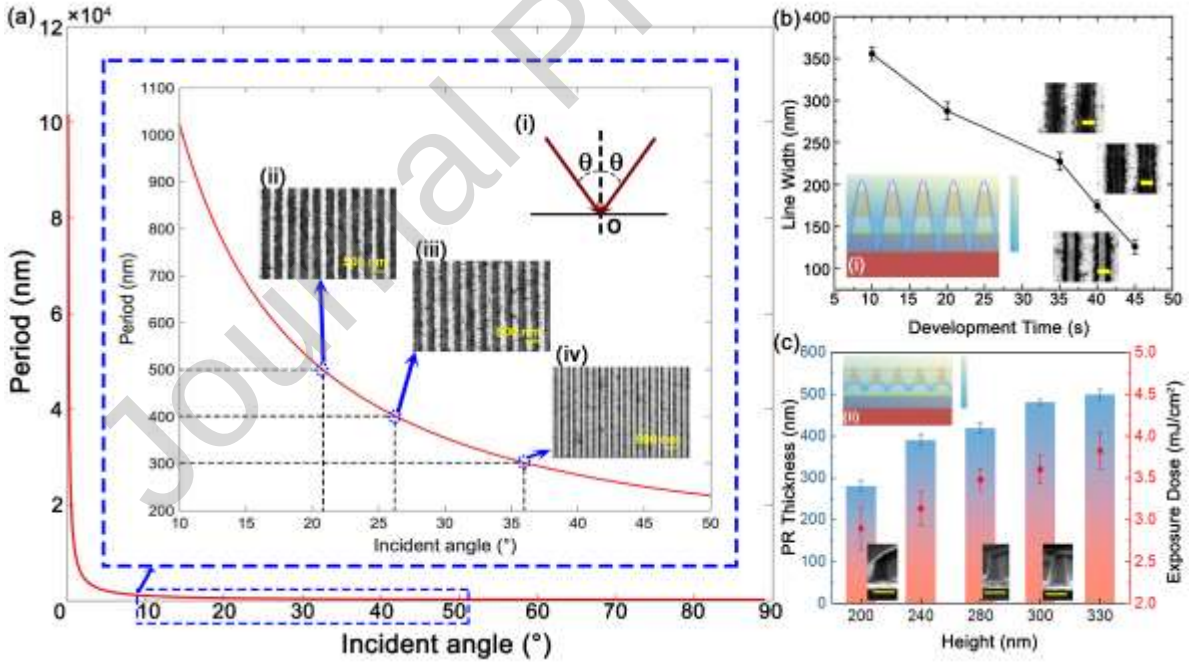

Fig. 2 Experimental results of periodic stripes fabrication by LIL. (a) Structural periods as a function of incident angles. (i) Incident angle (θ) of the laser beams; (ii-iv) SEM images of the structures with periods of 500 nm (ii), 400 nm (iii), and 300 nm (iv). (b-c) Relationship between structural morphology and etching parameters. Scale bar = 200 nm.

4. Results and Discussion

4.1 Design and Analysis of SERS Substrates

To investigate the SERS properties of micro-nano structures with heterogeneous multilayers, we simulate and test the periodic striped structures with Ag/SiO_2 layers, Ag/Au layers, and Ag/SiO_2/Au layers, as shown in Fig. 3. The three-dimensional schematics of the structures in the X-Z view are provided in Figs. 3a-c. The geometric parameters are defined in Fig. 3c, where P is the structural period, L is the line width of the developed PR stripe, H is the height of the developed PR stripe, and T is the thickness of the Ag layer. A cross-sectional view and a three-dimensional perspective view of the FDTD computational model for the periodic striped Ag/SiO_2/Au structure are provided in Fig. 3d.

For the Ag/SiO_2 structure shown in Fig. 3e, enhanced electric fields are observed near the Ag surfaces and within the stripe grooves, with part of the field extending into the dielectric layer. For the Ag/Au structure shown in Fig. 3f, the enhanced fields are mainly concentrated near the Ag surfaces and stripe edges. In Fig. 3c, the Ag/SiO_2/Au multilayers constitute a MIM-type vertical structure. The enhanced electric fields are distributed near the Ag surfaces and stripe edges, within the groove regions, and inside the dielectric spacer.

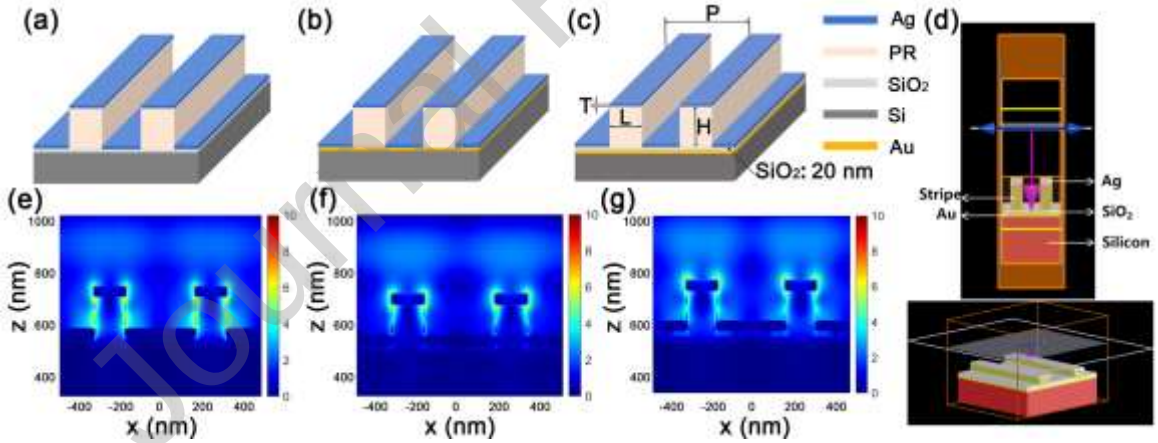

Fig. 3 FDTD simulations of the configuration of the MIM-type vertical structure. (a–c) Three-dimensional schematics of the Ag/SiO_2, Ag/Au, and Ag/SiO_2/Au structures, respectively. (d) FDTD simulation model of the periodic striped Ag/SiO_2/Au structure. (e-g) Electric field distributions on the x-z plane of (a-c), respectively.

Fig. 4a shows the absorption spectra of three substrate configurations, which supports the distinct functions of the Ag active layer, SiO_2 spacer, and Au reflective layer in the periodic striped MIM structure. Compared with the other structures, the periodic striped MIM structure exhibited the highest absorption response. The absorption peaks of 67.3%, 71.5%, and 70.7% are observed at 420 nm, 522 nm, and 646 nm, respectively, indicating strong resonant coupling within the structure. Ag was selected as the exposed plasmonic layer based on its wavelength-dependent optical response and its ability to support localized surface

plasmon excitation under 532-nm illumination [27]. As shown in Fig. 3g and Fig. 4b, the periodic Ag-coated stripes concentrate the electromagnetic field near the stripe edges and groove regions, where the analyte molecules directly interact with the plasmonically active surface. The plasmonic resonance of Ag-based hybrid arrays with the excitation light can strengthen light–matter interactions and enhance the SERS response [28]. In the $Ag/SiO_2/Au$ configuration, the Au layer is located beneath the SiO_2 spacer and functions as a reflective back layer rather than the molecule-contacting active surface. Reflection from the Au layer and interference within the multilayer structure redirect part of the downward-propagating optical energy toward the active region and reinforce optical-field confinement [16, 29]. This coupling structure demonstrated superior electromagnetic field enhancement, enabling maximum signal amplification at specific wavelengths [30]. When the incident light interacts with the periodic stripes, and the generated diffraction orders can match the waveguide mode of the planar waveguide and coupled into the waveguide layer (the insulating layer), thereby inducing guided-mode resonance. Within the insulating layer, interference between the incident and reflected light forms a standing wave, leading to strong localization of the electric field [29]. This configuration further promotes the coupling between the surface plasmon wave and the incident light, thereby enhancing Raman scattering.

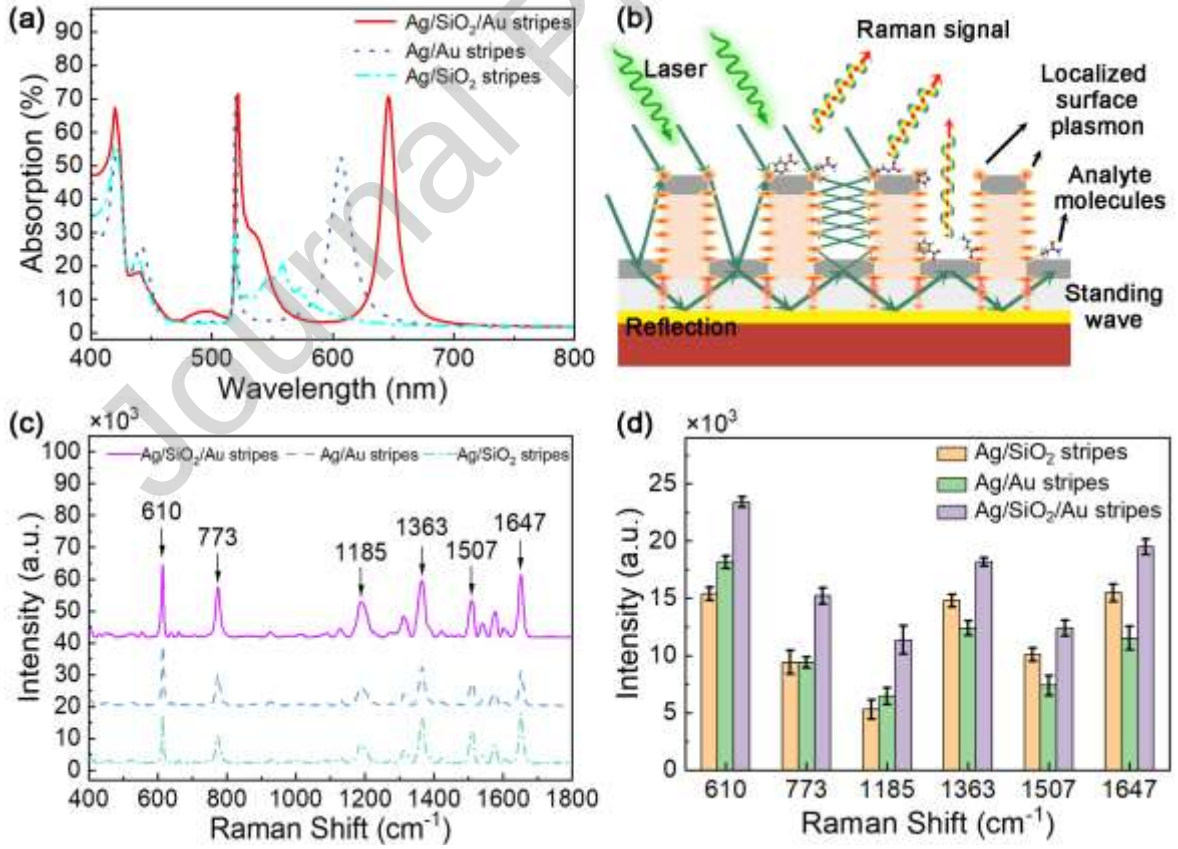

Fig. 4 (a) Absorption spectra of the three substrate configurations. (b) Schematic diagram of localized surface plasmon excitation in the periodic striped MIM structure under laser illumination. (c) Raman spectra testing of the substrates. (d) Histogram of signal intensities for the characteristic peaks of the

Journal Pre-proof

substrates.

Raman spectra of the structures are shown in Figs. 4c-d. Using the characteristic peak at 610 cm^{-1} as a reference, the periodic striped Ag/SiO_2/Au structure exhibits the highest Raman intensity. The result supports the proposed functions of the exposed Ag layer as the plasmonically active surface and the underlying SiO_2/Au layers in reinforcing optical-field confinement, as shown in Fig. 3g and Fig. 4b. The combined effects of plasmonic resonance, multilayer interference, and the periodic stripe geometry contribute to the enhanced SERS response. Quantitative analysis at 610 cm^{-1} peak under the MIM structure is presented in Fig. 4d, showing good agreement between the experimental measurements and simulation results.

The influence of structural parameters on the SERS performance of periodic striped MIM structures was systematically investigated, as shown in Fig. 5. The SiO_2 spacer thickness was fixed at 20 nm throughout this study to investigate the effects of P, L, H, and T under identical dielectric-spacer conditions. Although the SiO_2 thickness may affect the electromagnetic coupling in the MIM structure [29], its thickness dependence was not systematically investigated in the present work.

When the structural period approaches the excitation wavelength of 532 nm, a resonance effect can be induced, leading to enhanced electromagnetic fields on the nanostructured surface and consequently improving the Raman scattering signals of the adsorbed analyte molecules [30]. The FDTD results in Fig. 5a show a pronounced absorption resonance near 532 nm at P = 500 nm, which corresponds well with the strongest Raman response observed experimentally (Fig. 5b). The stripe line width (L) affects the SERS performance mainly through two aspects [31]. First, it modulates the electromagnetic field distribution around the stripes, thereby influencing the Raman enhancement of the molecular. Second, variations in line width can shift in the resonant wavelength, affecting its matching with the incident excitation wavelength. The simulated absorption map in Fig. 5c shows enhanced absorption within 500–550 nm for L ≈ 145–165 nm, together with a red shift of the resonance as L increases, which agrees with the strongest Raman signals are obtained at L = 150-160 nm in Fig. 5d. The H determines the vertical relief of the patterned surface and the spatial arrangement of the Ag-coated regions. The simulated absorption map in Fig. 5e exhibits a pronounced absorption region within 500–550 nm for H ≈ 200–230 nm, consistent with the strongest experimental response among the tested heights in Fig. 5f. Based on the simulated Ag/SiO_2/Au striped structure shown in Fig. 3g, the Ag thickness (T) affects plasmonic response and multilayer optical interference. The simulated absorption map in Fig. 5g shows high-absorption regions near the excitation wavelength at T ≈ 35–45 nm and 55–65 nm. An appropriate Ag thickness can effectively excite surface plasmon resonance, thereby enhancing the Raman scattering signal. By comparing the Raman intensity of the characteristic peak at 610 cm^{-1}, the optimal enhancement is achieved when the thickness is 40 nm or 60 nm, as shown in Fig. 5h. With the fixed SiO_2 spacer thickness of 20 nm, favorable

SERS performance was obtained for P = 500 nm, L = 150–160 nm, H = 200–230 nm, and T = 40 or 60 nm among the investigated parameter ranges.

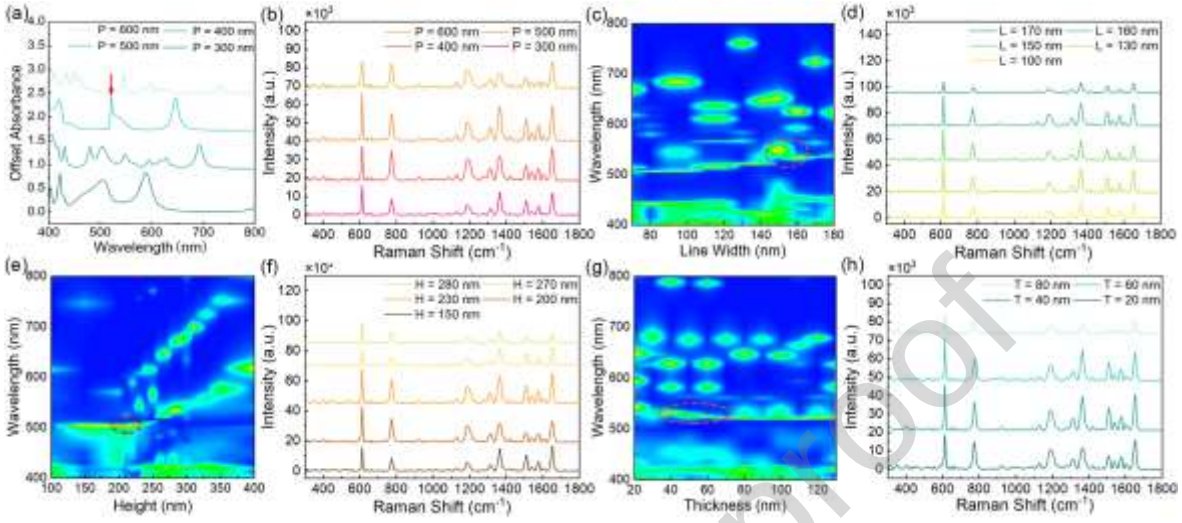

Fig. 5 FDTD simulations and Raman spectra of periodic striped MIM structures with diverse parameters. (a-b) Period (P). (c-d) Line width (L). (e-f) Height (H). (g-h) Thickness of the Ag layer (T).

4.2 Sensitivity of the periodic striped MIM structures

The enhancement factor (*EF)* is a key parameter for evaluating the performance of the SERS substrates. When the experimental parameters, including excitation power and integration time, are kept consistent, the *EF* can be simplified as [9]:

$$EF = \frac{I_{SERS}}{I_0} \cdot \frac{N_0}{N_{SERS}} \tag{1}$$

Where, I_{SERS} and I_0 represent the signal intensities adsorbed on the enhanced substrate and the silicon substrate (deposited with 50 nm Au film), while N_{SERS} and N_0 correspond to the number of molecules excited on the SERS-active surface and in conventional Raman testing. The formulas for calculating the number of molecules are listed below:

$$N_{SERS} = \sigma \times A \tag{2}$$

$$N_0 = C \times NA \times V = C \times NA \times A \times h \tag{3}$$

Where the surface coverage density (σ) is calculated to be 1.247×10^9 molecules/cm^2 based on the adsorption characterization results of R6G molecules. The laser spot area (A) is 5.309×10^{-8} cm^2. The concentration of R6G aqueous solution (C) is 10^{-4} M. The Avogadro constant (NA) is 6.022×10^{23} mol^{-1}. The effective solution depth (h), determined by the 10X objective focal length of 10.6 mm, represents the laser penetration depth. According to Eq. (1), using the five-time averaged Raman intensity of R6G molecules at 610 cm^{-1} (23700 counts for signal, 75 counts for background) measured on the periodic striped MIM structure, the *EF* is calculated to be 1.62×10^{10}.

To evaluate the detection sensitivity, R6G solutions with concentrations from 10^{-4} to 10^{-8} M were prepared by ten-fold dilution method and measured using the SERS substrate, as illustrated in Fig. 6. The characteristic Raman peaks of R6G remain clearly observable even at concentrations as low as 10^{-8} M. Regarding the calculation of the *LOD*, the formula is typically expressed as [32]:

$$LOD = 3\delta / S \tag{4}$$

Where the δ denotes the blank noise standard deviation, and the S indicates the slope of the signal intensity versus analyte concentration calibration curve. In this work, five measurements of blank signals yield a standard deviation of 14.13 counts, referenced to the silicon peak of at 520 cm^{-1}. The calibration curve established from Fig. 6a exhibited a slope of 1.92×10^8 counts/M based on the R6G peak at 610 cm^{-1}. According to Eq. (4), the calculated LOD was 2.2×10^{-7} M, and the lowest R6G concentration detected experimentally was 10^{-8} M. These results demonstrate the strong Raman enhancement and good sensing performance of the proposed periodic striped MIM substrate.

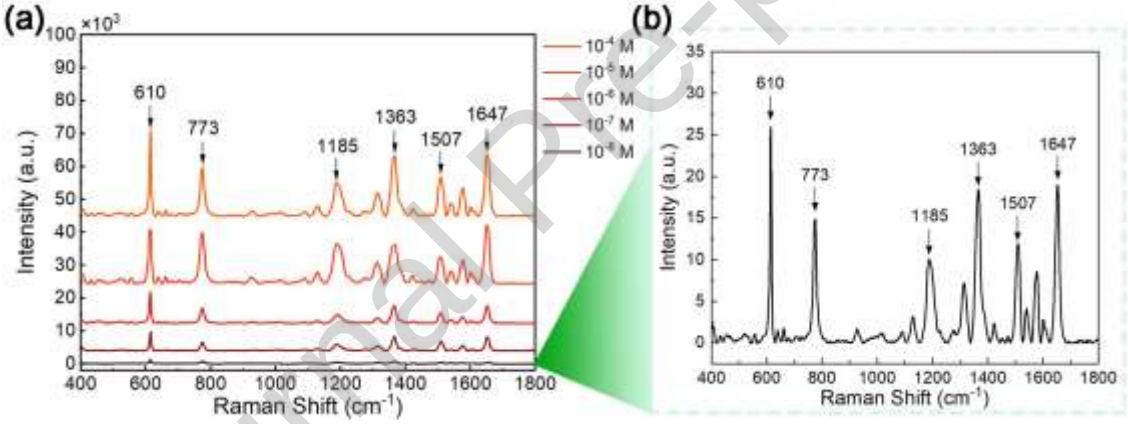

Fig. 6 Detection limit of the periodic striped MIM structures. (a) Raman spectra at various concentrations of R6G. (b) Raman spectrum corresponding to a R6G concentration of 10^{-8} M.

4.3 Uniformity, reproducibility, stability of the periodic striped MIM structures

Uniformity, reproducibility, and stability are critical factors for validating SERS properties. As shown in Fig. 7a, Raman measurements were collected from ten randomly selected positions on the substrate surface of the striped MIM structure, as marked by the colored circles in the inset. The relative standard deviation (RSD) of the characteristic peaks at 610, 773, 1185, 1363, 1507, and 1647 cm^{-1} are all below < 7% (Fig. 7b), indicating good signal consistency among the sampled positions. Although full Raman mapping would provide a more comprehensive assessment of spatial uniformity, the present multi-point measurements provide quantitative evidence for the uniform SERS response of the substrate.

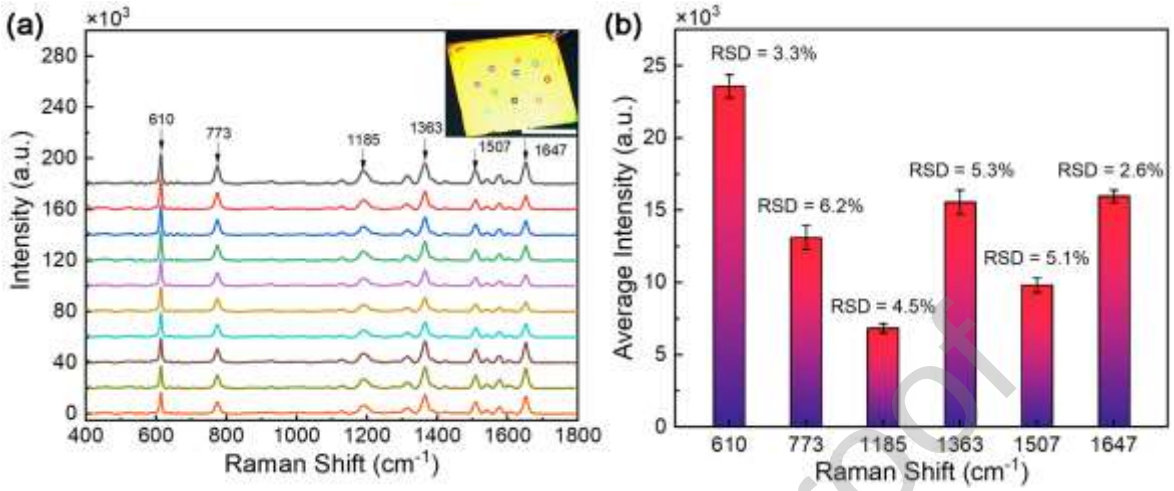

Fig. 7 Uniformity test of the periodic striped MIM structures. (a) Raman spectra measured at ten different locations on the same sample, scale bar = 5 mm. The corresponding spectra are shown in matching colors. (b) Histogram of signal intensities for different characteristic peaks of the sample.

Samples with identical geometric parameters (A-E) were randomly selected for Raman spectra testing and comparison, as shown in Fig. 8a, where the inset in the upper left corner displayed physical images of the five samples. The results show slight variations in the characteristic peak intensities, ranging between 22,200 a.u. to 23,700 a.u. In Fig. 8b, the inter-sample RSD values were below 13%, indicating good reproducibility among the substrate samples.

The long-term stability of the SERS substrate was evaluated over ten weeks using the samples. During this period, the substrate was stored in a sample box under controlled cleanroom conditions at 20–25 °C and approximately 20–25% relative humidity. Before each weekly measurement, the substrate was re-immersed in R6G solution. Each data point in Fig. 8c represents the average of three measurements. The characteristic Raman peak intensities gradually decreased with increasing storage time. A previous study of silver-coated periodic gratings showed that temperature or humidity variations alone caused relatively mild deterioration in SERS performance, while the combined action of temperature and humidity resulted in considerably stronger degradation [33]. The stable temperature and low humidity used in the present study may therefore have limited the environmental degradation of the exposed Ag layer. All the monitored characteristic peaks remained detectable after ten weeks, indicating that the substrate retained its SERS functionality under the specified storage and repeated-measurement conditions.

Journal Pre-proof

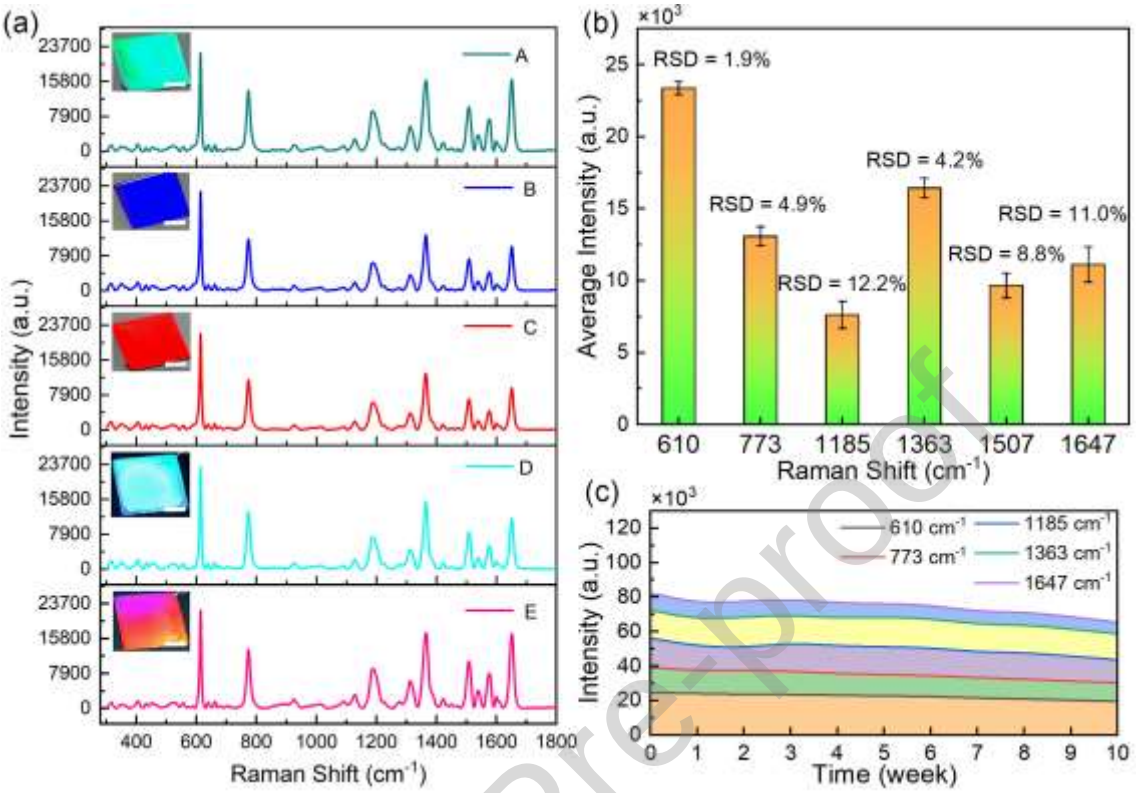

Fig. 8 Reproducibility and stability tests of the periodic striped MIM structures. (a) Raman spectra obtained from the samples (A–E) with identical geometric parameters at the same R6G concentration, scale bar = 5 mm. (b) Average characteristic Raman peak intensities and corresponding inter-sample RSD values calculated from (a). (c) Variation in the characteristic Raman peak intensities of the same substrate over ten weeks.

4.4 SERS-Microfluidic Device and Applications

Convenience and efficiency pose significant challenges that need to be addressed when applying the SERS platform to real-world problems [34-35]. In this work, by integrating the SERS substrate and a microfluidic chip, we have developed a detection device characterized by excellent performance, including convenience, safety, low dosage requirements, and real-time liquid analysis capabilities, as shown in Fig. 9a. By placing the SERS substrate at the bottom of the test chamber within the device, a microchannel is designed to pass through the test chamber, allowing the tested liquid to enter the chamber steadily. Given its cost-effective preparation process and relatively high SERS enhancement potential, the periodic striped MIM structures have been evaluated for its applicability in practical scenarios. In this work, melamine and malachite green are selected as analytes for the validation.

Melamine is illegally used as a food additive, the combination of melamine with its analogues, can lead to serious health issues, including kidney failure and even death in infants [36]. Fig. 9b displays the Raman spectra from the SERS-microfluidic device for

detecting melamine, along with illustrations of the chemical structure formula of melamine and its aqueous solutions. The Raman peak at 676 cm^{-1} is attributed to the ring breathing mode II, which corresponds to the in-plane deformation of the triazine ring [36]. Additionally, the C-N-C or N-C-N torsional vibrations of the triazine ring produce another peak at 984 cm^{-1} [37]. Although the SERS response of the proposed substrate toward melamine is relatively limited at low concentrations, weak characteristic peaks remain detectable at 10^{-4} M, confirming the feasibility of the SERS-microfluidic strategy for melamine identification. A calibration curve was established based on the results of Fig. 9b using the characteristic peak of melamine at 676 cm^{-1} as a reference, yielding a slope of 1.0 × 10^4 counts/M. According to Eq. (4) the calculated LOD for melamine was 4.2 × 10^{-3} M, while 10^{-4} M was the lowest melamine concentration detected experimentally.

Malachite green is a water-soluble dye widely used in aquaculture to prevent parasitic and fungal infections in fish [9]. However, it poses potential health risks due to its mutagenic and teratogenic effects. Its reliable detection is of great importance for preventing food safety hazards associated with illegal usage and for safeguarding public health. The Raman spectra of malachite green solutions with different concentrations are conducted using the SERS-microfluidic device, as shown in Figs. 9c-d. The characteristic peaks at 1180, 1591, and 1619 cm^{-1} are assigned to in-plane aromatic C-H bending vibrations, out-of-plane C-C stretching vibrations of the aromatic ring, and C-N stretching vibrations, respectively [38]. As the concentration of the malachite green analyte decreases, the SERS intensity gradually declines. When the concentration of malachite green solution reaches 10^{-6} M, it becomes increasingly challenging for the SERS-microfluidic device to detect its characteristic peaks, as shown in Fig. 9d. A calibration curve is established based on the data in Fig. 9c using the characteristic peak of malachite green at 1619 cm^{-1} as the reference, yielding a slope of 5.32 × 10^6 counts/M. According to Eq. (4), the calculated LOD for malachite green was 7.9 × 10^{-6} M, while 10^{-6} M was the lowest malachite green concentration detected experimentally.

Journal Pre-proof

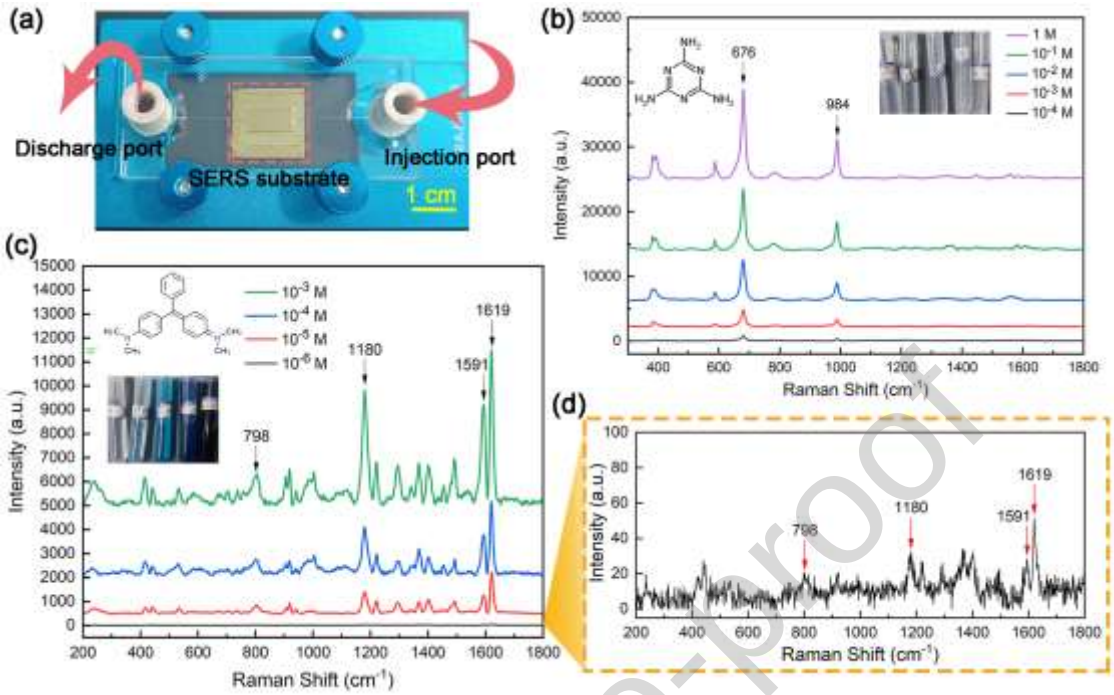

Fig. 9 (a) Schematic of the SERS-microfluidic device. (b-c) Raman spectra of melamine (b) and malachite green (c) at various concentrations dropped onto the SERS-microfluidic device. (d) Raman spectrum of malachite green at a concentration of 10^{-6} M.

Based on the principles of microfluid dynamics [39], the solution can flow steadily through the microchannels, facilitating distribution of analyte molecules over the periodic striped MIM structures. The SERS-microfluidic device was developed to combine molecular transport with Raman signal enhancement. The detection results for melamine and malachite green demonstrate the feasibility of the proposed platform for sensing food-safety-related analytes under controlled conditions. Although the present study provides proof-of-concept validation of the integrated sensing strategy, further investigations using a broader range of target analytes and complex real sample matrices are required to comprehensively evaluate its practical applicability.

To further evaluate the analytical performance and fabrication characteristics of the proposed SERS-microfluidic device, recently reported microfluidic SERS platforms were compared, as summarized in Table 1. Since these studies used different analytes, sample matrices, excitation conditions, and methods for determining the detection limit, the reported analytical values are presented for general comparison.

Table 1. Comparison of the analytical performance and fabrication characteristics of recently reported microfluidic SERS platforms.

Ref.	SERS substrate / fabrication	LOD / lowest concentration	EF	Fabrication characteristics
[40]	Nanopatterned Ag/PET;	CV	～10^6	Large-area and high-throughput, but

	Roll-to-roll embossing & PVD	demonstrated at 10^{-12} M		relies on the expensive e-beam masters.
[41]	Pd–Au core–shell nanorods onto magnetic beads in pump-free chip	aM level in serum	—	Extremely sensitive, but relies on hairpin DNA, magnetic beads, Pd–Au nanorods and signal amplification.
[42]	Au nanoparticle arrays; Fs-laser nanoparticle implantation	<10 ppt	> 10^8	Particularly valuable because it uses the same MG analyte; high sensitivity but relies on precision fs-laser processing.
[43]	Porous SiC impregnated with AgNPs; Chemical synthesis	< 10^{-12} M	> 10^{13}	High-performance porous composite substrate; additional porous-material and AgNP preparation required.
[44]	Au nanorod arrays; Oblique angle deposition	10 pg/mL	—	Pump-free and rapid, but relies on antigen or antibody and SERS tags.
[45]	3D core-shell Ag–SiO_2 microsphere; Self-assembly	10^{-12} M for R6G	> 10^{10}	Comparatively simple self-assembly route, flexible substrate and pump-free operation, but relies on the cells, difficult to prepare large-area.
Our work	Periodic striped Ag/SiO_2/Au MIM; LIL & PVD/PECVD	10^{-8} M for R6G	> 10^{10}	Periodic patterning; suitable for low-cost and large-area fabrication; no biorecognition or biochemical signal-amplification process.

As summarized in Table 1, several recently reported microfluidic SERS platforms achieve lower detection limits than the present device. However, many of these highly sensitive approaches rely on complex nanofabrication processes, such as femtosecond-laser processing, or additional biochemical recognition and signal-amplification strategies involving antibodies, aptamers, magnetic particles, or Raman tags [40-45]. In comparison, the proposed periodic striped MIM substrate is fabricated by LIL, which enables patterning of periodic micro-nanostructures over a relatively large area. Although the present sensitivity toward melamine and malachite green remains moderate, the combination of a high SERS enhancement factor (1.62×10^{10}), relatively straightforward fabrication, and compatibility with microfluidic integration suggests its potential as a scalable SERS sensing platform.

5. Conclusion

In summary, this work presents periodic striped MIM structures as a SERS substrate that facilitates large-area and cost-effective fabrication by LIL, while ensuring the substrate production efficiency. The high sensitivity of the periodic striped MIM configuration in analyte detection can be predominantly ascribed to the two functions—surface plasmon resonance occurs onto the active layer and guided-mode resonance arises from interference phenomena within the plasmonic cavity. They synergistically contribute to the optimal enhancement of the Raman signal. The periodic striped Ag/SiO_2/Au structures demonstrate good SERS detection capability and reproducibility, which attain a detection limit of 10^{-8} M and an EF surpassing 10^{10}. Moreover, a microfluidic chip furnished with the SERS substrate is posed and detected melamine and malachite green. The LOD for malachite green reaches 7.9×10^{-6} M, validating the feasibility of the SERS-microfluidic device. In essence, this work puts forward an easy strategy for low-cost and large-area manufacturing of high resolution and reproducible biochemical sensors with exceptional SERS performance. The periodic line-grating structure promotes electric-field oscillations between the grooves, leading to enhanced field intensity.

Disclosures

The authors declare no conflicts of interest.

Data availability statement

The data that support the findings of this work are available upon reasonable request from the authors.

References

[1] H. Li, E. Dumont, R. Slipets, T. Thersleff, A. Boisen and G. A. Sotiriou, Democratizing robust SERS nano-sensors for food safety diagnostics, Chem. Eng. J. 470 (2023) 144023.

[2] J. Liu, X. Huang, X. Zhang, Y. Feng, Z. Yuan, S. Gao, Z. Li, H. S. El-Mesery, J. Shi, and X. Zou. Sensing technology empowering food safety: research progress of SERS-assisted multimodal biosensing toward food hazard factors, Anal. Methods, 17 (2025), 3083-3110.

[3] L. B. T. Nguyen, Y. X. Leong, C. S. L. Koh, S. X. Leong, S. K. Boong, H. Y. F. Sim, G. C. Phan-Quang, I. Y. Phang and X. Y. Ling, Inducing ring complexation for efficient capture and detection of small gaseous molecules using SERS for environmental surveillance, Angew. Chem. Int. 61 (33) (2022).

[4] X. Zhang, K. Zhao, X. Wang, H. Wang, W. Yang, J. Liu and D. Li, Surface-enhanced Raman spectroscopy for environmental monitoring using gold clusters anchored on reduced graphene oxide, Sci. Total Environ. 856 (2023).

[5] E.X. Tan, Y.X. Leong, S.H. Lim, M. W. K. Chng, I. Y. Phang, and X. Y. Ling. Chemistry-informed recommender system to predict optimal molecular receptors in SERS nanosensors. Nat. Commun. 16 (2025), 7095.

[6] D. Chen, J. Gao, D. He, J. He, Y. Li, M. Zhang, W. Li, X. Chen, X. He and T. Fu, Plasmonic bridge sensor enabled by carbon nanotubes and Au-Ag nano-rambutan for multifunctional detection of biomechanics and bio/chemical molecules, ACS Appl. Mater. Interfaces. 15 (6) (2023) 8783-8793.

[7] S. Xiang, X. Wang, Y. Pang, C. Ge, Y. Xu, L. Chen, S. Li and L. Wang, Porous Au/AAO: a simple and feasible SERS substrate for dynamic monitoring and mechanism analysis of DNA oxidation, Appl. Surf. Sci. 606 (2022) 154842.
[8] J. Zhang, C. Song, X. He, J. Liu, J. Chao and L.i Wang. DNA-mediated precise regulation of SERS hotspots for biosensing and bioimaging, Chem. Soc. Rev. 54 (2025) 5836-5863.
[9] P. Mandal and B. S. Tewari. Progress in surface enhanced Raman scattering molecular sensing: a review, Surf. Interfaces. 28 (2022) 101655.
[10] R. Wang, J. Ma, X. Dai, Y. Gao, C. Gu and T. Jiang, Highly active SERS chip with both structure-ameliorated chemical enhancement and nanocavity-mediated electromagnetic enhancement, Sens. Actuators B Chem. 374 (2023) 132782.
[11] M. Magdy, A conceptual overview of surface-enhanced Raman scattering (SERS), Plasmonics. 18 (2) (2023) 803-809.
[12] I. Shlesinger, I. M. Palstra and A. F. Koenderink, Integrated sideband-resolved SERS with a dimer on a nanobeam hybrid, Phys. Rev. Lett. 130 (1) (2023).
[13] W. Yue, T. Gong, X. Long, V. Kravets, P. Gao, M. Pu and C. Wang, Sensitive and reproducible surface-enhanced Raman spectroscopy (SERS) with arrays of dimer-nanopillars, Sens. Actuators B Chem. 322 (2020) 128563.
[14] G. Li, X. Zhao, X. Tang, L. Yao, W. Li, J. Wang, X. Liu, B. Han, X. Fan, T. Qiu and Q. Hao, Wearable hydrogel SERS chip utilizing plasmonic trimers for uric acid analysis in sweat, Nano Lett. 24 (42) (2024) 13447-13454.
[15] Y. Huang, R. Yang, T. Xiao, H. Li, M. Tian, Z. Xie, J. Zheng, J. Zhu, Y. Su, W. Chen, K. Liu, M. Tang and L. Li, Wafer-scale self-assembled 2.5D metasurface for efficient near-field and far-field electromagnetic manipulation, Appl. Surf. Sci. 601 (2022) 154244.
[16] F. Dai, A. Horrer, P. M. Adam and M. Fleischer, Accessing the hotspots of cavity plasmon modes in vertical metal-insulator-metal structures for surface enhanced Raman scattering, Adv. Opt. Mater. 8 (7) (2020) 1901734.
[17] J. Liu, L. Feng, Z. Li, Y. Wu, F. Zhou and Y. Xu, Plasma-etching on monolithic MOFs-based MIM filter boosted chemical sensing, Nano Res. 17 (4) (2023) 2800.
[18] J. Kim, H. Oh, B. Kang, J. Hong, J.-J. Rha and M. Lee, Broadband visible and near-infrared absorbers implemented with planar nanolayered stacks, ACS Appl. Nano Mater. 3 (3) (2020) 2978.
[19] W. Nam, J. Song, S. A. Safiabadi Tali, H. J. Lezec, A. Agrawal and W. Zhou, Au/SiO_2-nanolaminated plasmonic nanoantennas as refractive-index-insensitive and transparent surface-enhanced Raman spectroscopy substrates, ACS Appl. Nano Mater. 4 (3) (2021) 3175.
[20] M. Nie, Y. Zhao, W. Nam, J. Song, W. Zhu, H. J. Lezec, A. Agrawal and W. Zhou, Broadband nanoscale surface-enhanced Raman spectroscopy by multiresonant nanolaminate plasmonic nanocavities on vertical nanopillars, Adv. Funct. Mater. 32 (32) (2022) 2202231.
[21] S. Das, J.-C. Tinguely, V. Kundu, K. Saxena, B. S. Ahluwalia and D. S. Mehta, Sculptured silicon nanopillars bridging face to face nanogaps with metal-insulator-metal coating for surface enhanced Raman spectroscopy, Surf. Interfaces. 44 (2024) 103836.
[22] Y. Geng, Y. Gao, Y. Yan, J. Verma, C. Y. Chee, S. Zhang and J. Wang, Prediction of surface structure and optimization of corrosion resistance in magnesium alloys via machine learning for nanosecond laser processing, Surf. Interfaces. 81 (2026) 108407.
[23] M. Mikalkevičius, N. Khinevich, S. Tamulevičius, T. Tamulevičius and A. Tamulevičienė, Templated silver nanoparticle deposition on laser-induced periodic surface structures for SERS sensing, Surf. Interfaces. 51 (2024) 104603.
[24] K. Jiang, M. Xie, Z. Tang, X. Zhang and D. Yang, Large-area nanostructure fabrication with a 75 nm half-pitch using deep-UV flat-top laser interference lithography, Sensors. 25 (18) (2025) 5906.
[25] Y. Chai, F. Li, J. Wang, P. Karvinen, M. Kuittinen and G. Kang, Enhanced sensing performance from trapezoidal metallic gratings fabricated by laser interference lithography, Opt. Lett. 47 (4) (2022) 1009.
[26] X. Chai, Z. Weng, H. Zhong, M. Sun, J. Yang, J. Qiao, and X. Zhang. Laser interference lithography-defined electrochemical etching of ordered InP nanopore arrays, Nanoscale, 18(2026) 4821-4831.
[27] P. B. Johnson and R. W. Christy, Optical constants of the noble metals, Phys. Rev. B 6 (12) (1972) 4370-4379.
[28] S. Deng, W. Dou, Y. Wu, M. Shao, C. Ji, J. Yu, C. Zhang, S. Xu, B. Man and Z. Li, Dual-tunable SERS substrate: synergistic enhancement via plasmonic resonance tailoring and pyroelectric field modulation in Ag/BTO hybrid arrays, Opt. Laser Technol. 203 (2026) 115468.
[29] K. Liu, T. Gong, Y. Luo, W. Kong, W. Yue, C. Wang and X. Luo, Ultrasensitive enhanced Raman spectroscopy by hybrid surface-enhanced and interference-enhanced Raman scattering with metal-

insulator-metal structures, Opt. Express. 31 (10) (2023) 15848.
[30] N. Khinevich, M. Juodėnas, A. Tamulevičienė, T. Tamulevičius, M. Talaikis, G. Niaura and S. Tamulevičius, Wavelength-tailored enhancement of Raman scattering on a resonant plasmonic lattice, Sens. Actuators B Chem. 394 (2023) 134418.
[31] A. O. Sweedan, M. J. Pavan, E. Schatz, H. Maaß, A. Tsega, V. Tzin, K. Höflich, P. Mörk, T. Feichtner and M. Y. Bashouti, Evolutionary optimized, monocrystalline gold double wire gratings as a novel SERS sensing platform, Small. 20 (35) (2024) 2470262.
[32] K. Cao, M. Wu, E. Wang, C. Liu, H. Zhu, C. Ma and J. Cao, Dual-mode SPR/SERS biosensor utilizing metal nanogratings fabricated via wet etching-assisted direct laser interference patterning, Appl. Surf. Sci. 655 (2024) 159621.
[33] Y. Kalachyova, D. Mares, V. Jerabek, R. Elashnikov, V. Švorčík and O. Lyutakov, Longtime stability of silver-based SERS substrate in the environment and (bio)environment with variable temperature and humidity, Sens. Actuators A Phys. 285 (2019) 566-572.
[34] W. Dai, X. Xia, X. Ding, X. Wei, X. Zhu, W. xue, Z. Hou and Y. Cao, Enhancing microfluidic chip functionality via thermal gradient-driven optofluidic manipulation, Adv. Mater. Technol. 9 (11) (2024) 2301986.
[35] L. Wang, C. Li, C. Cao, F. Lei, X. Zhao, Z. Li, C. Zhang, Y. Jiao and J. Yu, Multifunctional polymeric nanoneedles with “full-spectrum intrinsic internal standard” for precise SERS biosensing, Adv. Funct. Mater. 35 (10) (2025) 2416789.
[36] M. Tiwari, A. Singh, S. Dureja, S. Basu and S. K. Pattanayek, Au nanoparticles decorated ZnO/$ZnFe_2O_4$ composite SERS-active substrate for melamine detection, Talanta. 236 (2022) 122819.
[37] C. Huang, S. Jiang, F. Kou, M. Guo, S. Li, G. Yu, B. Zheng, F. Xie, C. Zhang, H. Yu and J. Wang, Development of jellyfish-like ZnO@Ag substrate for sensitive SERS detection of melamine in milk, Appl. Surf. Sci. 600 (2022) 154153.
[38] X. Dou, L. Zhao, X. Li, L. Qin, S. Han and S.-Z. Kang, Ag nanoparticles decorated mesh-like MoS_2 hierarchical nanostructure fabricated on Ti foil: a highly sensitive SERS substrate for detection of trace malachite green in flowing water, Appl. Surf. Sci. 509 (2020) 145331.
[39] A. George, F. Akbaridoust, N. A. Zainal Abidin, W. S. Nesbitt and I. Marusic, Characterisation of hydrodynamic trapping in microfluidic cross-slot devices for high strain rate applications, Lab Chip. 23 (13) (2023) 3092-3105.
[40] Y. Gutiérrez, M. Losurdo, I. Prinz, A. Prinz, G. Bauer, M. Bauer, M. M. Schmidt and T. Schaller, Paving the way to industrially fabricated disposable and customizable surface-enhanced Raman scattering microfluidic chips for diagnostic applications, Adv. Eng. Mater. 24 (8) (2022) 2101365.
[41] X. Cao, S. Ge, X. Zhou, Y. Mao, Y. Sun, W. Lu and M. Ran, A dual-signal amplification strategy based on pump-free SERS microfluidic chip for rapid and ultrasensitive detection of non-small cell lung cancer-related circulating tumour DNA in mice serum, Biosens. Bioelectron. 205 (2022) 114110.
[42] Y. Hu, Y. Zhou, G. Luo, D. Li and M. Qu, Femtosecond laser-induced nanoparticle implantation into flexible substrate for sensitive and reusable microfluidics SERS detection, Int. J. Extrem. Manuf. 6 (4) (2024) 045005.
[43] P. Wang, C. Yi, L. Wang, Y. Zhang and Q. Liao, 3D porous silicon carbide SERS microfluidic chip for pesticide residue detection, ACS Agric. Sci. Technol. 4 (8) (2024) 818-826.
[44] S. Xiong, C. Zhu, C. Wang, P. Dong and X. Wu, SERS-based pump-free microfluidic chip sensor for highly sensitive competitive immunoassay of cortisol in human sweat, Lab Chip 24 (24) (2024) 5384-5397.
[45] P. Wang, C. Yi, Y. Zhang, Y. Sun, P. Tang, Q. Liao and Y. Xiong, Flexible Ag-SiO2 microsphere SERS substrate integrated microfluidic chip for fungal pathogen detection in rapeseed crop, Food Chem. 491 (2025) 145178.

Declaration of Competing Interest

The authors declare that they have no known competing financial interests or personal

relationships that could have appeared to influence the work reported in this paper.

Acknowledgments

This work is supported by National Key R&D Program of China (No. 2023YFE0108900), Jilin Provincial Science and Technology Program (No. YDZJ202501ZYTS601), Horizon Europe Program (L4DNANO, No. 101086227), Zhongshan Social Welfare & Basic Research Program (No. 220427204368325), Zhongshan Innovative Research Team Project (No. CXTD2023003), and "111" Project of China (No. D17017).

Highlights:

• LIL enables straightforward, low-cost fabrication of large-area SERS chips.

• Periodic nano-stripe Ag/SiO_2/Au structures strengthen local electromagnetic fields.

• SERS substrate with periodic stripe MIM structures achieves an EF exceeding 10^{10}.

• Integrating MIM substrates with microfluidics enables real-time, in situ detection.

Journal Pre-proof